PROCEEDINGS OF THE ROYAL SOCIETY A

Proc. R. Soc. A (2010) **466**, 283–301
doi:10.1098/rspa.2009.0262
Published online 14 October 2009

Nonlinear secondary whirl of an overhung rotor

By K. Nandakumar* and Anindya Chatterjee

Mechanical Engineering, Indian Institute of Science, Bangalore 560012, India

Gravity critical speeds of rotors have hitherto been studied using linear analysis, and ascribed to rotor stiffness asymmetry. Here, we study an idealized asymmetric *nonlinear* overhung rotor model of Crandall and Brosens, spinning close to its gravity critical speed. Nonlinearities arise from finite displacements, and the rotor's static lateral deflection under gravity is taken as small. Assuming small asymmetry and damping, slow modulations of whirl amplitudes are studied using the method of multiple scales. Inertia asymmetry appears only at second order. More interestingly, even without stiffness asymmetry, the gravity-induced resonance survives through geometric nonlinearities. The gravity resonant forcing does not influence the resonant mode at leading order, unlike the typical resonant oscillations. Nevertheless, the usual phenomena of resonances, namely saddle–node bifurcations, jump phenomena and hysteresis, are all observed. An unanticipated periodic solution branch is found. In the three-dimensional space of two modal coefficients and a detuning parameter, the full set of periodic solutions is found to be an imperfect version of three mutually intersecting curves: a straight line, a parabola and an ellipse.

Keywords: gravity critical speed; overhung rotor; stiffness asymmetry; multiple scales; periodic solution

1. Introduction

Asymmetric rotors exhibit interesting phenomena such as unstable speed ranges between critical speeds (e.g. Smith 1933; Yamamoto & Ōta 1963), gravity critical speeds (Den Hartog 1956; Rao 1983) and nonlinearity-induced additional resonances (e.g. Yamamoto *et al.* 1982; Ishida *et al.* 2008). In addition, stator asymmetry can create new instabilities while modifying the existing ones owing to rotor asymmetry (e.g. Foote *et al.* 1943; Brosens & Crandall 1961). Ishida (1994) gave an excellent overview of nonlinear phenomena in rotor dynamics. Several other relevant papers are listed in the electronic supplementary material.

Here, we focus on gravity-induced resonances in perfectly balanced overhung rotors, sometimes called Stodola–Green rotors (Childs 1993). Gravity-induced resonances occur in slightly asymmetric rotors at about half of the mean flexural

*Author for correspondence (nandakumar.1979@gmail.com).

Electronic supplementary material is available at http://dx.doi.org/10.1098/rspa.2009.0262 or via http://rspa.royalsocietypublishing.org.

Received 13 May 2009
Accepted 15 September 2009

critical speed (Smith 1933). The relevant literature primarily identifies these gravity critical speeds (Coleman & Feingold 1958; Brosens & Crandall 1961; Genta 2005), with subsequent linear analyses under various idealizations: Jeffcot rotor models on rigid bearings (Taylor 1940; Childs 1993; Rajalingham *et al.* 1993; Genta 2005), Jeffcot rotors on flexible pedestals (Kondo & Kimura 1991), Euler–Bernoulli beam models (Bishop & Parkinson 1965; Sakata *et al.* 1983) and three-dimensional finite element (FE) models (Rao & Sreenivas 2003). Experimental results on horizontal cantilever shafts were reported, for example, by Hull (1961), and on a simply supported shaft with a centrally mounted wheel were reported by Bishop & Mahalingam (1965).

Studies of nonlinear behaviour near gravity critical speeds of overhung rotors are, somewhat surprisingly, absent from the literature. Two exceptions are Ishida *et al.* (2008) and Nagasaka *et al.* (2008), but they studied shafts supported at both ends. Ishida *et al.* (2008) studied internal resonances in an asymmetric shaft with a centrally mounted disc near both the primary and the gravity critical speeds; bearing clearances introduced nonlinearities. Nagasaka *et al.* (2008) studied the $1:-1$ internal resonance (between forward and backward whirl modes) in a simply supported, slender, asymmetric shaft near both the primary and the secondary critical speeds; note that the resonance effectively presupposes small gyroscopic effects. In contrast, we studied an overhung rotor with significant gyroscopic effects and non-infinitesimal deflections. We used the method of multiple scales (MMS) (see Thomsen (1995) and references therein) up to second order, with some problem-specific adaptation, while Ishida *et al.* (2008) and Nagasaka *et al.* (2008) used the method of averaging up to first order.

In this paper, we report on our studies of the idealized overhung rotor model of Crandall & Brosens (1961). In that work, linear equations were written, gravity was ignored and a linear stability analysis pointed out, for example the unstable gap between primary whirl speeds. Here, we write nonlinear equations for finite displacements. Linearization yields the correct gravity critical speed. Subsequently, for spin near the gravity critical speed, we use the MMS for a detailed study. We remark that the model discussed here, if fabricated exactly, might have low practical use (in addition to nonlinear effects we will ignore here). Overhung rotors where the end-loaded shaft passes through a bearing are far more common. However, models for such rotors would require at least two more degrees of freedom, and so we have focused here on the simplest possible overhung rotor model from the literature.

2. System description

The rotor model of Crandall & Brosens (1961) is shown in figure 1. Let XYZ represent the inertial coordinate system, with unit vectors $\mathbf{i}$, $\mathbf{j}$ and $\mathbf{k}$. Gravity acts along $-\mathbf{j}$ as shown. The horizontal input shaft spins at a constant rate Ω about $\mathbf{k}$, and in turn spins the nominally horizontal, overhung output shaft through a massless universal joint made of two yokes and a cross-piece with centre O, as shown. The output shaft is rigid, and massless but for the disc of mass M at its end. The disc, the output shaft and yoke A are collectively called 'the rotor', and its length is l.

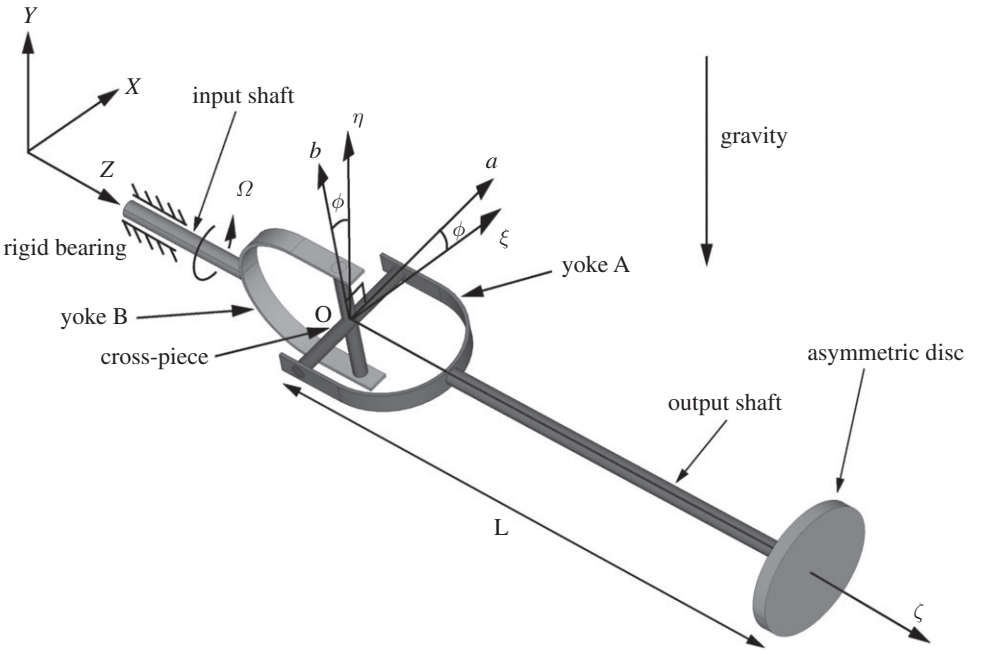

Figure 1. Schematic of overhung rotor model of Crandall & Brosens (1961).

The rotor has two rotational degrees of freedom. Let unit vectors **a** and **b** be defined as shown in figure 1. Let $\bar{\theta}_a$ and $\bar{\theta}_b$ be the rotations about **a** and **b**. These rotations are resisted by torsion springs of stiffnesses K_a and K_b, respectively. We assume $K_a \geq K_b$. Weak torsional dashpots in parallel with the torsion springs provide energy dissipation.

For kinetic energy calculations, we will use the rotor's moment of inertia matrix about point O. Let the principal axes of that matrix be ξ–η–ζ with I_ξ, I_η being the diametral and I_ζ being the polar moments of inertia, respectively. For an asymmetric rotor, $I_\xi \neq I_\eta$. We assume $I_\xi \geq I_\eta$. When $\bar{\theta}_a = \bar{\theta}_b = 0$, the inertia axes ξ–η make an angle ϕ with the stiffness axes **a**–**b** (see the figure).

3. Equations of motion

Linearized equations of motion derived by Lagrange's method using body-fixed axes ($\xi\eta\zeta$) were presented in Crandall & Brosens (1961). Here, our derivation of the nonlinear equations of motion begins with laboratory-fixed coordinates XYZ, and our representation of rotation matrices mimics that in Basu-Mandal *et al.* (2007). In particular, we will make repeated use of an axis-angle formula as described below.

We choose and hold a single set of coordinate axes (XYZ) fixed, so that vectors are equivalent to their matrices of components. Now, on rotating any rigid body through an angle ψ about a unit vector **n**, any vector **r** embedded in the body is transformed (rotated) to the vector **r**′ given by $\mathbf{r}' = \mathbf{R}(\mathbf{n}, \psi)\mathbf{r}$, where

$$\mathbf{R}(\mathbf{n}, \psi) = \cos\psi\mathbf{I} + (1 - \cos\psi)\mathbf{n}\mathbf{n}^{\mathrm{t}} + \sin\psi\mathbf{S}(\mathbf{n}),$$

where in turn the t-superscript denotes matrix transpose and $\mathbf{S}(\mathbf{n})$ is the skew-symmetric cross-product matrix.[1] All rotations of all bodies will be viewed as successive rotations of the above form; angular velocities of bodies will be extracted from the time derivatives of rotation matrices; the moment of inertia matrix calculations will also use these same rotation matrices; and when the system kinetic and potential energies are known, it remains to model the dissipation and then Lagrange's equations can be written routinely. Some further details are provided in the electronic supplementary material.

Here, we merely say that the rotor's kinetic energy is finally written as

$$T = \frac{1}{2}\omega^{\mathrm{t}}\mathbf{I}_{XYZ}\omega. \tag{3.1}$$

The potential energy arises from the torsion springs and gravity and is given by

$$\begin{aligned} V &= \frac{1}{2}K_a\bar{\theta}_a^2 + \frac{1}{2}K_b\bar{\theta}_b^2 + Mgl(\mathbf{R}_{\mathrm{net}}\mathbf{k})\cdot\mathbf{j} \\ &= \frac{1}{2}K_a\bar{\theta}_a^2 + \frac{1}{2}K_b\bar{\theta}_b^2 + Mgl\sin(\Omega t)\cos\bar{\theta}_a\sin\bar{\theta}_b \\ &\quad - Mgl\cos(\Omega t)\sin\bar{\theta}_a, \end{aligned} \tag{3.2}$$

where $\mathbf{R}_{\mathrm{net}}$ is the net rotation matrix and g is the acceleration owing to gravity.

We now turn to dissipation, which we model through viscous, torsional damping at the pivots in the universal joint. The generalized dissipation forces for $\bar{\theta}_a$ and $\bar{\theta}_b$, denoted by $\mathcal{F}_a$ and $\mathcal{F}_b$, are, respectively,

$$\mathcal{F}_a = -c\,\dot{\bar{\theta}}_a \quad \text{and} \quad \mathcal{F}_b = -c\,\dot{\bar{\theta}}_b,$$

where c is a common coefficient.

Finally, the Lagrangian is $\mathcal{L} = T - V$, and Lagrange's equations are

$$\frac{\mathrm{d}}{\mathrm{d}t}\left(\frac{\partial\mathcal{L}}{\partial\dot{\bar{\theta}}_a}\right) - \left(\frac{\partial\mathcal{L}}{\partial\bar{\theta}_a}\right) = -c\,\dot{\bar{\theta}}_a \tag{3.3}$$

and

$$\frac{\mathrm{d}}{\mathrm{d}t}\left(\frac{\partial\mathcal{L}}{\partial\dot{\bar{\theta}}_b}\right) - \left(\frac{\partial\mathcal{L}}{\partial\bar{\theta}_b}\right) = -c\,\dot{\bar{\theta}}_b. \tag{3.4}$$

The full expressions, obtained using the symbolic algebra package MAPLE, are long and not reproduced here.

4. Linearization

We introduce the following symbols for ease of presentation:

$$I_m = \left(\frac{I_\xi + I_\eta}{2}\right), \quad I_d = \left(\frac{I_\xi - I_\eta}{2}\right), \quad K_m = \left(\frac{K_a + K_b}{2}\right), \quad K_d = \left(\frac{K_a - K_b}{2}\right).$$

[1] $\mathbf{S}(\mathbf{n})\mathbf{u} = \mathbf{n}\times\mathbf{u}$ for all $\mathbf{n}$ and $\mathbf{u}$.

Thus, I_m represents the mean diametral mass moment of inertia, while I_d represents inertia asymmetry; and K_m represents the mean stiffness, while K_d represents stiffness asymmetry. Using the above, the linearization of equations (3.3) and (3.4) yields

$$\mathbf{A}\ddot{\bar{\boldsymbol{\Theta}}} + (\mathbf{B}+\mathbf{E})\dot{\bar{\boldsymbol{\Theta}}} + \mathbf{C}\bar{\boldsymbol{\Theta}} = \mathbf{F}, \tag{4.1}$$

where $\bar{\boldsymbol{\Theta}} = \begin{Bmatrix}\bar{\theta}_a \\ \bar{\theta}_b\end{Bmatrix}$, $\mathbf{F} = \begin{Bmatrix} Mgl\cos(\Omega t) \\ -Mgl\sin(\Omega t)\end{Bmatrix}$ and the coefficient matrices

$$\mathbf{A} = \begin{bmatrix} I_m + I_d\cos 2\phi & -I_d\sin 2\phi \\ -I_d\sin 2\phi & I_m - I_d\cos 2\phi\end{bmatrix}, \quad \mathbf{B} = \Omega(I_\zeta - 2I_m)\begin{bmatrix}0 & 1\\ -1 & 0\end{bmatrix}$$

and

$$\mathbf{C} = \begin{bmatrix} \Omega^2(I_\zeta - I_m + I_d C_{2\phi}) + K_m + K_d & -\Omega^2 I_d S_{2\phi} \\ -\Omega^2 I_d S_{2\phi} & \Omega^2(I_\zeta - I_m - I_d C_{2\phi}) + K_m - K_d\end{bmatrix},$$

where $C_{2\phi}$ and $S_{2\phi}$ denote $\cos 2\phi$ and $\sin 2\phi$, respectively; and $\mathbf{E}$ is simply c times the 2×2 identity matrix. Note that $\mathbf{A}$ is the inertia matrix, $\mathbf{B}$ adds gyroscopic terms, $\mathbf{E}$ adds damping and $\mathbf{C}$ is an effective stiffness matrix. However, if we ignore gravity and seek synchronous whirl solutions, then we must use $\det(\mathbf{C}) = 0$, showing that some gyroscopic *effects* are included in $\mathbf{C}$ as well. Mahadevan *et al.* (2008) discussed this issue for continuum rotors.

Moving on, following Crandall & Brosens (1961), we introduce

$$\epsilon_i = \frac{I_d}{I_m}, \quad \epsilon_s = \frac{K_d}{K_m}, \quad J = \frac{I_\zeta}{I_m}, \quad \tau = \Omega t, \quad \sigma = \frac{\Omega}{\sqrt{K_m/I_m}},$$

where ϵ_i and ϵ_s are non-dimensional inertia and stiffness asymmetries, respectively, J represents the source of gyroscopic effects if any, τ is non-dimensional time and σ is non-dimensional spin speed. Note that $0 \le \epsilon_i < 1$, $0 \le \epsilon_s < 1$, $0 < J < 2$ and $0 \le \phi \le \pi/2$. At the extremes, which we avoid, $J = 0$ for a point mass at the shaft tip, while $J = 2$ for a centrally pivoted zero-thickness disc (i.e. $l = 0$).

Substituting the above definitions in equation (4.1) and simplifying, we have

$$\bar{\mathbf{A}}\bar{\boldsymbol{\Theta}}'' + (\bar{\mathbf{B}}+\bar{\mathbf{E}})\bar{\boldsymbol{\Theta}}' + \bar{\mathbf{C}}\bar{\boldsymbol{\Theta}} = \bar{\mathbf{F}}, \tag{4.2}$$

where primes denote derivatives with respect to τ,

$$\bar{\mathbf{A}} = \begin{bmatrix} 1+\epsilon_i\cos 2\phi & -\epsilon_i\sin 2\phi \\ -\epsilon_i\sin 2\phi & 1-\epsilon_i\cos 2\phi\end{bmatrix}, \quad \bar{\mathbf{B}} = (J-2)\begin{bmatrix}0 & 1\\ -1 & 0\end{bmatrix},$$

$$\bar{\mathbf{C}} = \begin{bmatrix} J-1+\epsilon_i\cos 2\phi + (1+\epsilon_s)/\sigma^2 & -\epsilon_i\sin 2\phi \\ -\epsilon_i\sin 2\phi & J-1-\epsilon_i\cos 2\phi + (1-\epsilon_s)/\sigma^2\end{bmatrix}$$

and $\bar{\mathbf{E}} = \dfrac{c}{\sigma\sqrt{K_m I_m}}\begin{bmatrix}1 & 0\\ 0 & 1\end{bmatrix}$ and $\bar{\mathbf{F}} = \dfrac{Mgl}{K_m\sigma^2}\begin{Bmatrix}\cos\tau \\ -\sin\tau\end{Bmatrix}$.

5. Undamped gravity critical speed

We initially ignore the damping and consider the homogeneous equation

$$\bar{\mathbf{A}}\bar{\boldsymbol{\Theta}}'' + \bar{\mathbf{B}}\bar{\boldsymbol{\Theta}}' + \bar{\mathbf{C}}\bar{\boldsymbol{\Theta}} = \mathbf{0}. \tag{5.1}$$

The characteristic equation of (5.1) is of the form $\alpha\lambda^4 - 2\beta\lambda^2 + \gamma = 0$, where the α, β and γ we obtain (we have checked) match Crandall & Brosens (1961). Synchronous whirl corresponds to $\lambda = 0$. However, here we are interested in gravity critical speeds. According to Brosens & Crandall (1961) and Coleman & Feingold (1958), for an asymmetric two degrees of freedom rotor, there are four natural frequencies for each spin speed. At the gravity critical speed, one of these frequencies vanishes, whence constant gravity can excite the corresponding mode. That same condition corresponds to $\lambda = 1$ in our treatment because our generalized coordinates are defined in a rotating system. Setting $\lambda = 1$ in the above characteristic equation and solving for Ω, we obtain

$$\Omega_{\mathrm{gc}} = \sqrt{\frac{K_m}{I_m}}\sqrt{\frac{1-\epsilon_s^2}{4-2J}}. \tag{5.2}$$

If stiffness asymmetry and J are *both* small, $\Omega_{\mathrm{gc}} \approx 1/2\sqrt{K_m/I_m}$, as has been noted by many others. Also, inertia asymmetry and the angle ϕ have no effect on the gravity critical speed (as stated by Smith 1933). In our nonlinear analysis, however, inertia asymmetry will have a weak (second-order) effect.

6. Method of multiple scales

We observe in $\bar{\mathbf{F}}$ of equation (4.2) the parameter Mgl/K_m, the static angular deflection under self-weight, which is typically small; we will use this parameter in our multiple scales expansion. Lagrange's equations (3.3) and (3.4) involve trigonometric terms. We will expand them in power series (up to fifth power). We further define

$$\sqrt{\nu} = \frac{Mgl}{K_m}, \quad \bar{\theta}_a = \sqrt{\nu}\theta_a, \quad \bar{\theta}_b = \sqrt{\nu}\theta_b, \quad \epsilon_i = \nu\delta$$

and

$$\epsilon_s = \nu\kappa, \quad c = \nu\mu\sqrt{K_m I_m}, \quad \sigma = \frac{1}{\sqrt{4-2J}} + \nu\Delta,$$

where $0 < \nu \ll 1$; where θ_a, θ_b, κ, δ, μ and Δ are $\mathcal{O}(1)$ quantities; and where Δ represents detuning or deviation from the leading order expression for gravity critical speed. Note that asymmetries, as well as damping, have been taken to be one order smaller than the static deflection of the rotor.

A consequence of such scaling is that, unlike typical near-resonance analyses of weakly nonlinear oscillators (see Nayfeh & Mook 1979, pp. 163–173), the forcing from gravity will appear at leading order itself in the analysis below. Technically, this is possible without the blow-up of terms because the resonant forcing does not directly excite the corresponding resonant mode in this two degrees of freedom

system. Physically and intuitively, the near axisymmetric nature of the rotor diminishes the magnitude of the response, thus allowing the rotor to tolerate relatively larger forcing.

Expanding for small $\sqrt{\nu}$ and then dividing through by $\sqrt{\nu}$, and on replacing primes by overdots to better match the convention for time derivatives (understanding that overdots now signify τ-derivatives), we finally have

$$\mathbf{P}\ddot{\boldsymbol{\Theta}} + \mathbf{Q}\dot{\boldsymbol{\Theta}} + \mathbf{R}\boldsymbol{\Theta} = \mathbf{f} + \nu\mu\mathbf{D}\dot{\boldsymbol{\Theta}} + \nu(\mathbf{N_1} + \mathbf{N_2}) + \nu^2\mathbf{N_3}, \tag{6.1}$$

where $\boldsymbol{\Theta} = \begin{Bmatrix}\theta_a \\ \theta_b\end{Bmatrix}$, $\mathbf{f} = (4-2J)\begin{Bmatrix}\cos\tau \\ -\sin\tau\end{Bmatrix}$ and the coefficient matrices

$$\mathbf{P} = \begin{bmatrix}1 & 0 \\ 0 & 1\end{bmatrix}, \quad \mathbf{Q} = (J-2)\begin{bmatrix}0 & 1 \\ -1 & 0\end{bmatrix}$$

and

$$\mathbf{R} = \begin{bmatrix}3-J & 0 \\ 0 & 3-J\end{bmatrix} \quad \text{and} \quad \mathbf{D} = -\sqrt{4-2J}\begin{bmatrix}1 & 0 \\ 0 & 1\end{bmatrix}.$$

The term $\mathbf{N_1} = \{N_{11}, N_{12}\}^{\mathrm{t}}$ contains harmonic forcing terms and terms linear in the generalized coordinates and their derivatives; these terms, though linear, represent small effects (as denoted by the ν premultiplier). The term $\mathbf{N_2} = \{N_{21}, N_{22}\}^{\mathrm{t}}$ contains cubic nonlinearities (such as θ_a^3 and $\dot{\theta}_b\theta_a^2$), as well as quadratically nonlinear parametric forcing terms (such as $\theta_a\theta_b\sin\tau$ and $\theta_a^2\cos\tau$). Finally, the term $\mathbf{N_3} = \{N_{31}, N_{32}\}^{\mathrm{t}}$ contains a combination of forcing, linear and nonlinear terms up to fifth order. Further details are given in the electronic supplementary material.

We now proceed to apply the MMS to equation (6.1), and begin with a first-order analysis.

We first rewrite the equations in a state space form as

$$\dot{\mathbf{X}} = \mathbf{M}\mathbf{X} + \mathbf{G}(\tau) + \nu\mathbf{H}(\mathbf{X}, \tau) + \nu^2\mathbf{W}(\mathbf{X}, \tau), \tag{6.2}$$

where the state vector $\mathbf{X} = \begin{Bmatrix}\theta_a \\ \dot{\theta}_a \\ \theta_b \\ \dot{\theta}_b\end{Bmatrix}$,

$$\mathbf{M} = \begin{bmatrix}0 & 1 & 0 & 0 \\ J-3 & 0 & 0 & 2-J \\ 0 & 0 & 0 & 1 \\ 0 & J-2 & J-3 & 0\end{bmatrix}, \quad \mathbf{G}(\tau) = (4-2J)\begin{Bmatrix}0 \\ \cos\tau \\ 0 \\ -\sin\tau\end{Bmatrix},$$

and $\mathbf{H}$ and $\mathbf{W}$ incorporate asymmetry, detuning, damping and nonlinearities.

We introduce multiple time scales: $T_0 = \tau$, $T_1 = \nu\tau$, $T_2 = \nu^2\tau, \ldots$ and write

$$\mathbf{X} = \mathbf{X}_0(T_0, T_1, T_2, \ldots) + \nu\mathbf{X}_1(T_0, T_1, T_2, \ldots) + \nu^2\mathbf{X}_2(T_0, T_1, T_2, \ldots) + \cdots. \tag{6.3}$$

Substituting equation (6.3) in equation (6.2) and taking time derivatives as is usual for the MMS, we have at $\mathcal{O}(1)$

$$\frac{\partial \mathbf{X}_0}{\partial T_0} = \mathbf{M}\mathbf{X}_0 + (2-J)\begin{Bmatrix} 0 \\ 1 \\ 0 \\ i \end{Bmatrix} e^{iT_0} + (2-J)\begin{Bmatrix} 0 \\ 1 \\ 0 \\ -i \end{Bmatrix} e^{-iT_0}, \tag{6.4}$$

where $\mathbf{G}(\tau)$ has been written using complex exponential notation.

Now, the eigenvalues of $\mathbf{M}$ are $i, -i, i(J-3), -i(J-3)$, with $J \neq 2$. Thus, the harmonic forcing could *potentially* excite unbounded responses along eigenvectors corresponding to the eigenvalues $\pm i$. It turns out that it does not. This issue is a key aspect of the present analysis. In view of its importance here, we pause to consider a general system

$$\dot{\mathbf{x}} = \mathbf{A}\mathbf{x} + \mathbf{u}\, e^{\lambda t}.$$

If λ is *not* an eigenvalue of $\mathbf{A}$, then there is a solution of the form $\mathbf{x} = \mathbf{b}\, e^{\lambda t}$, found easily by solving $(\mathbf{A} - \lambda\mathbf{I})\mathbf{b} = -\mathbf{u}$, where $\mathbf{I}$ is the identity matrix and $\mathbf{A} - \lambda\mathbf{I}$ is not singular because λ is not an eigenvalue. In contrast, if λ is in fact an eigenvalue of $\mathbf{A}$, then the coefficient matrix is singular and there is in general no bounded solution for $\mathbf{b}$. In the *special case* where $\mathbf{u}$ lies in the column space of $\mathbf{A} - \lambda\mathbf{I}$, or equivalently when $\mathbf{u}$ is orthogonal to the left null vector of $\mathbf{A} - \lambda\mathbf{I}$, then there are bounded but non-unique solutions for $\mathbf{b}$. The non-uniqueness consists of an arbitrary scalar multiple of the *right* null vector of $\mathbf{A} - \lambda\mathbf{I}$. In our MMS analysis, the situation is the last one, with bounded but non-unique solutions at first order.

Thus, the solution for $\mathbf{X}_0$ is bounded and non-unique. Intuitively, as the gravity resonance is mainly due to asymmetries which are absent at this order, we expect no unbounded solutions here. The lack of immediately unbounded solutions resembles, for example, the dynamics of a straight rod excited torsionally at a bending natural frequency. In this way, our system differs from the usual resonantly forced, weakly nonlinear oscillators where no primary-resonance forcing can be sustained at leading order.

Proceeding with our analysis, the solution of equation (6.4) contains a complementary solution and a particular integral. The particular integral, as discussed above, is non-unique. Moreover, the non-unique portion can be absorbed into the complementary solution involving the eigenvalues $\pm i$. Thus, the solution of equation (6.4) is

$$\begin{aligned}\mathbf{X}_0(T_0, T_1, T_2) = {} & (c_1(T_1, T_2) + ic_2(T_1, T_2))\begin{Bmatrix} 1 \\ i \\ -i \\ 1 \end{Bmatrix} e^{iT_0} + \begin{Bmatrix} 1 \\ i \\ 0 \\ 0 \end{Bmatrix} e^{iT_0} \\ & + (c_1(T_1, T_2) - ic_2(T_1, T_2))\begin{Bmatrix} 1 \\ -i \\ i \\ 1 \end{Bmatrix} e^{-iT_0} + \begin{Bmatrix} 1 \\ -i \\ 0 \\ 0 \end{Bmatrix} e^{-iT_0}. \end{aligned} \tag{6.5}$$

We have not included the contribution of the eigenvalue $i(J-3)$ in the complementary solution as it is neither resonantly forced (as $J \neq 2$) nor involved in any internal resonances (as we have verified; details not presented here), and hence will be eventually damped out. The real-valued functions $c_1(T_1, T_2)$ and $c_2(T_1, T_2)$ are to be determined from calculations at subsequent orders.

Proceeding to the next order, at $\mathcal{O}(\nu)$ we have

$$\frac{\partial \mathbf{X}_1}{\partial T_0} - \mathbf{M}\mathbf{X}_1 = -\frac{\partial \mathbf{X}_0}{\partial T_1} + \mathbf{H}(\mathbf{X}_0, T_0). \tag{6.6}$$

Substituting equation (6.5) in the right-hand side of equation (6.6), we have

$$\begin{aligned}\frac{\partial \mathbf{X}_1}{\partial T_0} - \mathbf{M}\mathbf{X}_1 = {} & \mathbf{U}(T_1, T_2)\, e^{iT_0} + \bar{\mathbf{U}}(T_1, T_2)\, e^{-iT_0} + \mathbf{V}(T_1, T_2)\, e^{3iT_0} \\ & + \bar{\mathbf{V}}(T_1, T_2)\, e^{-3iT_0},\end{aligned} \tag{6.7}$$

where the overbars denote complex conjugates, and where $\mathbf{U}$ and $\mathbf{V}$ involve complicated expressions (not presented) in terms of c_1, c_2, their partial derivatives with respect to T_1, along with system parameters.

In equation (6.7), as before, we encounter forcing in resonance with the eigenvalues $\pm i$. To eliminate secular terms, we must ensure (as discussed above) that $\mathbf{U}$ is orthogonal to the left eigenvector of $\mathbf{M}$ corresponding to the eigenvalue i (e.g. Thomsen 1995), with a corresponding condition for $\bar{\mathbf{U}}$ being then identically satisfied. Thus, the solvability conditions may be written compactly as

$$\mathbf{U}^{\mathrm{t}}(T_1, T_2) \begin{Bmatrix} -i \\ \dfrac{1}{J-3} \\ 1 \\ \dfrac{i}{J-3} \end{Bmatrix} = 0. \tag{6.8}$$

Separating the real and imaginary parts of equation (6.8), we obtain after elementary manipulations the slow flow equations (dependencies on T_1 and T_2 suppressed for simplicity)

$$\begin{aligned}\frac{\partial c_1}{\partial T_1} = {} & \frac{1}{2J-8}(16c_2 + 24c_2^3 + 24c_2c_1 + 8\sqrt{4-2J}\Delta Jc_2 - 13Jc_2 + 24c_1^2c_2 \\ & - 22Jc_1^2c_2 - 24Jc_2c_1 - 16\sqrt{4-2J}\Delta c_2 + 2\sqrt{4-2J}\mu c_1 \\ & + \sqrt{4-2J}\mu - 22Jc_2^3)\end{aligned} \tag{6.9}$$

and

$$\begin{aligned}\frac{\partial c_2}{\partial T_1} = {} & \frac{1}{2J-8}(-6 - 4\kappa + 5J + 12Jc_2^2 - 24c_2^2c_1 + 23Jc_1 + 36Jc_1^2 + 22Jc_2^2c_1 \\ & + 8\sqrt{4-2J}\Delta - 36c_1^2 - 12c_2^2 - 24c_1^3 + 22Jc_1^3 - 24c_1 + 2\kappa J \\ & + 16\sqrt{4-2J}\Delta c_1 - 4\sqrt{4-2J}\Delta J + 2\sqrt{4-2J}\mu c_2 - 8\sqrt{4-2J}\Delta Jc_1).\end{aligned} \tag{6.10}$$

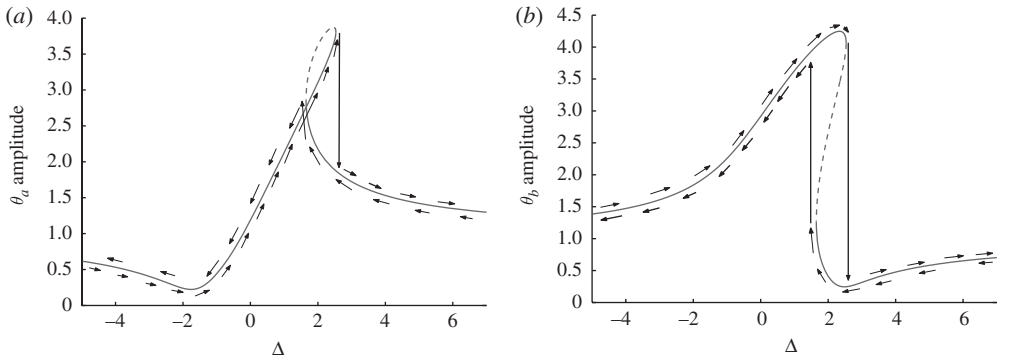

Figure 2. Multiple periodic solutions, both stable and unstable, can coexist. Transitions from stable to unstable portions occur at points where tangents are vertical (at $\Delta \approx 2.53$ and $\Delta \approx 1.65$). Parameters: $\kappa = 7$, $\mu = 3$ and $J = 0.5$. (a,b) Black line, stable; dashed line, unstable.

The above equations govern, up to first order, the evolution of whirling solution amplitudes. We mention here that we have in fact proceeded to the next order (after solving equation (6.7)) and obtained expressions for $\partial c_1/\partial T_2$ and $\partial c_2/\partial T_2$. The second-order slow flow contains the inertia asymmetry parameter which is absent at first order, and provides better approximations than the first order. Details are presented in the electronic supplementary material for completeness.

For the current system, conducting a linearized analysis of the slow flow equations may be tricky. An examination of the first-order slow flow equations (6.9) and (6.10) shows that some terms which are seemingly linear, such as $16c_2$ of equation (6.9), and some constant terms as well, have their origin in the quadratically nonlinear terms in equation (6.1). Thus, linearization of *our* slow flow would generally not be equivalent to throwing away nonlinear terms right at the start. In other words, people may differ even on what the linearized equations are. Kane *et al.* (1987) contains a related discussion. For these reasons, we do not undertake a study of the simplified linearized equations and consider only the nonlinear slow flow.

7. Results: initial observations

The fixed points of the slow flow equations (equations (6.9) and (6.10), if working with first order) represent periodic solutions of equation (6.2). These slow flow equations will, by and large, be treated numerically below. Note that the numerical treatment of the slow flow is much faster than the direct numerical treatment of the original equation (6.2). We will use only the first-order slow flow for the most part, because it suffices for the qualitative dynamics we examine; for some parameter values, however, second-order equations do give greater accuracy, as we will illustrate below.

Before a detailed study of the slow flow, some preliminary numerical results are plotted in figure 2. From the fixed points of the first-order slow flow,

equations (6.9) and (6.10), the amplitudes of θ_a and θ_b are found from equation (6.5) as

$$\theta_a = 2\sqrt{(c_1+1)^2 + c_2^2}, \quad \theta_b = 2\sqrt{c_1^2 + c_2^2}. \tag{7.1}$$

The slow flow is also linearized about each fixed point, and eigenvalues of the linearized system are used to determine stability (as depicted in figure 2). Equilibrium solution branches are numerically computed using an arclength-based branch following scheme (see Nandakumar & Chatterjee 2005), as Δ is varied in parameter space. Saddle–node bifurcations, jump phenomena and hysteresis, familiar in nonlinear resonances, are all observed. The plot for θ_a appears to self-intersect in this view, but the underlying three-dimensional curve $(\theta_a - \theta_b - \Delta)$ does not self-intersect (see the plot for θ_b). A phase portrait for the above, with $\Delta = 2$, wherein three solutions coexist, is given in the electronic supplementary material. We now proceed to a more detailed investigation.

To compare the first- and second-order slow flows, we consider two sets of parameter values. In each case, the periodic solutions are computed in three ways: (i) by the direct treatment of equation (6.2)[2], (ii) from the first-order slow flow, equations (6.9) and (6.10), and (iii) from the second-order slow flow (long equations, not presented here). Results are plotted in figure 3. For the first case (corresponding to figure 3*a,b*), first and second orders are both of acceptable accuracy; while for the second case (corresponding to figure 3*c,d*), first order has somewhat poor accuracy. In both cases, second-order results are indistinguishable from full numerics within plotting accuracy. Henceforth, however, for computational ease and owing to our primary interest in the qualitative aspects of the dynamics, we will use the first-order slow flow alone.

We now summarize some other preliminary observations here.

Inertia asymmetry (δ) has no role in determining the gravity critical speed (see equation (5.2)) and only a weak influence on the amplitudes of resonant solutions, in that it is absent in the first-order slow flow, equations (6.9) and (6.10), and appears at second order.

Gyroscopic effects, represented by J, have a significant role in the gravity-induced resonant dynamics. Exploratory numerical results suggest that, for light damping, decreasing J eventually raises the maximum amplitudes.

Geometric nonlinearities, even in the absence of stiffness asymmetry, allow a somewhat weaker gravity-induced resonant response. The effect is attenuated by damping, and is in any case weaker than that of stiffness asymmetry.

Details are given in the electronic supplementary material. We now proceed to somewhat less familiar results.

8. Other periodic solution branches

To motivate this section, let us consider $\nu = 0.001$, $J = 0.6$, $\mu = 0.1$, $\delta = 0$, $\phi = \pi/3$ and $\kappa = 1$. Numerical results from the first-order slow flow are plotted in figure 4. In figure 4, in addition to the usual stable–unstable–stable primary

[2]Periodic solutions of equation (6.2), or even the full equations (3.3) and (3.4) (which we have done as well, but do not report here because they lead to no visible difference), are found iteratively through shooting methods and a numerical implementation of the Newton–Raphson method.

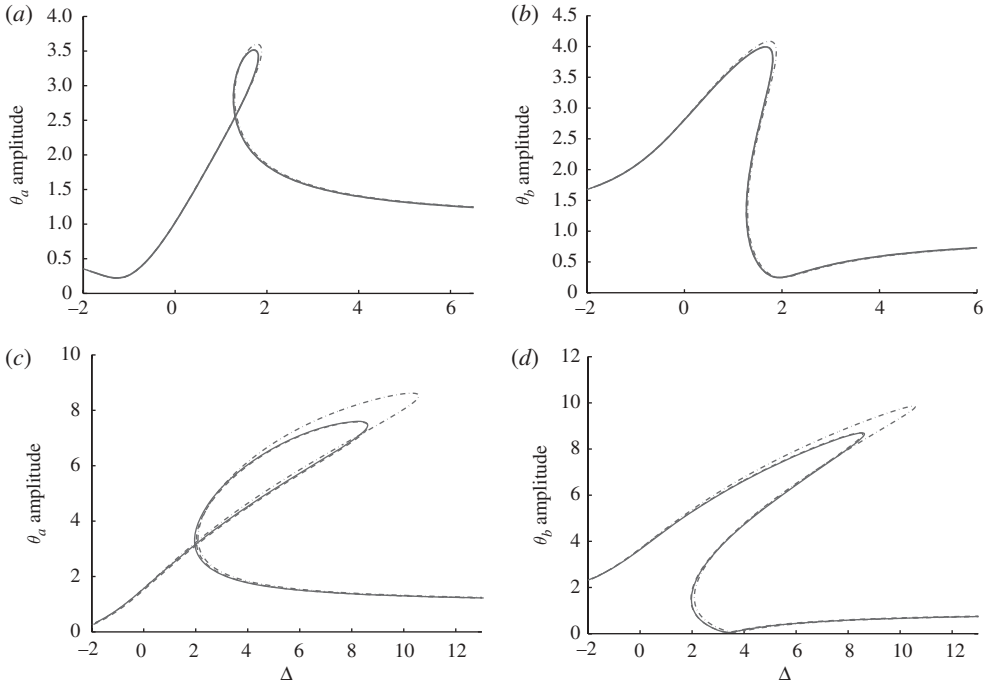

Figure 3. Comparison of first-order and second-order slow flows. (*a*,*b*) Parameters are $\nu = 0.002$, $\kappa = 5$, $\delta = 2$, $\mu = 2$, $\phi = \pi/5$ and $J = 0.7$; (*c*,*d*) parameters are $\nu = 0.003$, $\kappa = 10$, $\delta = 2$, $\mu = 1$, $\phi = \pi/5$ and $J = 0.7$. (*a*–*d*) Solid line, direct numerics; dot–dash line, first-order MMS; dashed line, second-order MMS.

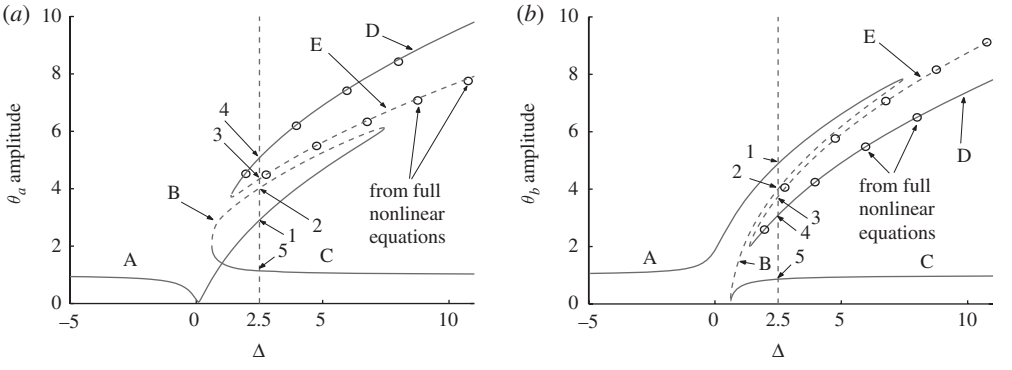

Figure 4. Additional periodic solution branches. Parameters: $\nu = 0.001$, $\delta = 0$, $\kappa = 1$, $\mu = 0.1$, $\phi = \pi/3$ and $J = 0.6$. (*a*,*b*) Solid line, stable; dashed line, unstable.

branches A–B–C, we see additional stable–unstable branches D–E. As a check, we have also computed these additional periodic solutions from the full nonlinear equations (3.3) and (3.4) (i.e. with no series truncation at all, and incorporating ν, δ and ϕ as above) and plotted some of those using circles (o) in the same figure. Agreement is good enough that, for subsequent studies, only the MMS first-order slow flow is used.

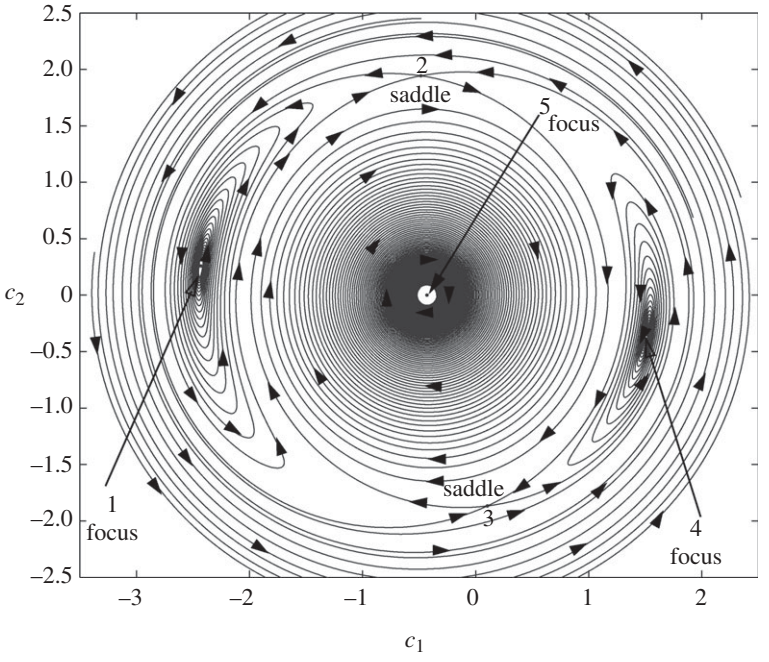

Figure 5. Phase portrait illustrating the coexistence of five periodic solutions. Parameters: $\kappa = 1$, $\mu = 0.1$, $\Delta = 2.5$ and $J = 0.6$.

A representative phase portrait at $\Delta = 2.5$, showing five coexisting solutions including three stable ones, is given in figure 5. It is clear that the primary stable solutions (marked 1 and 5) are foci in the portrait, while the primary unstable solution, marked 2, is a saddle. The secondary stable solution, marked 4, is also a focus while the secondary unstable solution, marked 3, is a saddle. The secondary focus possesses a significant basin of attraction, and the rotor could quite possibly settle on to that motion.

For higher damping, these additional solution branches recede from the primary branch. For sufficiently large damping, five coexisting periodic solutions are no longer possible (see the electronic supplementary material). Conversely, for lower damping, we expect the additional solution branch to exist for the values of Δ even closer to zero. To check this, we consider $\mu = 0.00001$ with all other parameters being the same as in figure 4. The resulting solution branches, this time in $c_1 - c_2 - \Delta$ space, are plotted in figure 6. For ease of identification, the various branches in figure 6 have been given the same labels as in figure 4.

The rest of this paper is essentially aimed at understanding figure 6. In the figure, for large negative values of Δ, we only have the solution branch A. For increasing Δ, A merges with branch B in a saddle–node bifurcation (see the zoomed view of the boxed portion in figure 7*b*). Following branch B, Δ now decreases until B merges with stable branch C in another saddle–node bifurcation. Subsequently, Δ increases indefinitely along C. On the remaining branches shown, which form another single curve, starting along the additional stable branch D

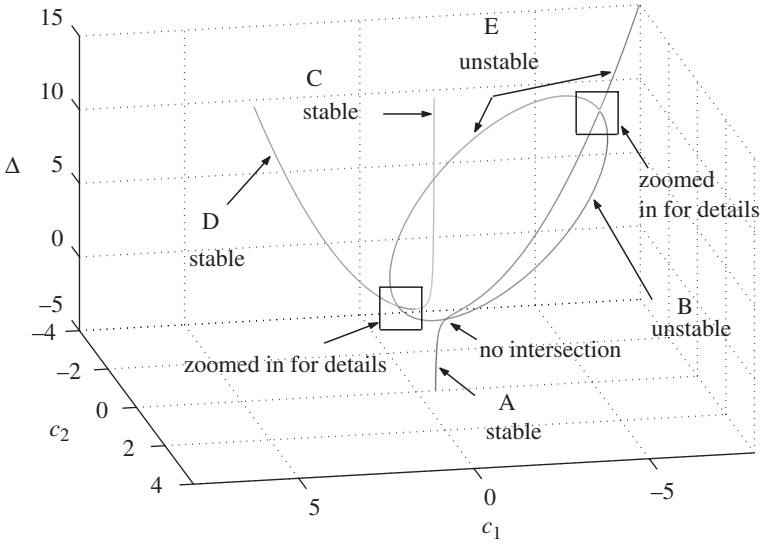

Figure 6. Solution branches at low damping showing the bifurcation structure. Parameters: $\kappa = 1$, $\mu = 0.00001$ and $J = 0.6$.

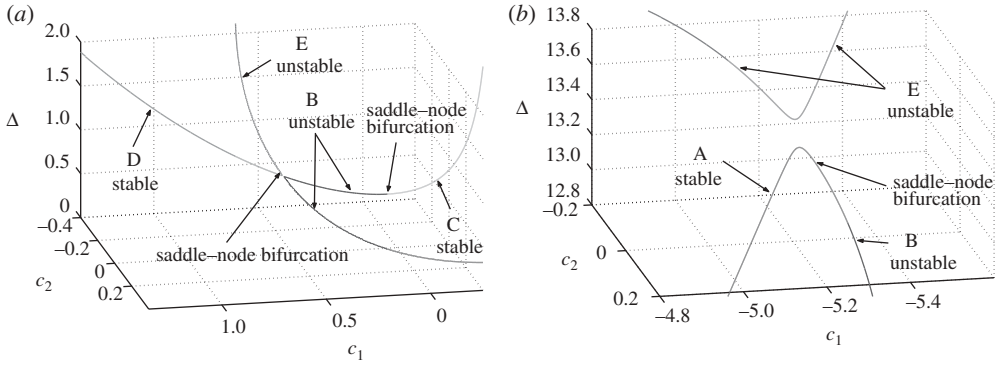

Figure 7. Zoomed portions of figure 6 near bifurcation points. (*a*) Zoomed-in view near the junction of branches D and E (left box in figure 6). (*b*) Zoomed-in view near the junction of branches A, B and E (right box in figure 6).

for large positive Δ, we encounter a saddle–node bifurcation where D merges with unstable branch E (see the zoomed view of the boxed portion in figure 7*a*). Continuing along E, Δ increases indefinitely.

In figure 6, it seems that branches E and B are the broken halves of an ellipse. We anticipate that, with damping $\mu = 0$, these branches do form an ellipse. To verify this, we generate the solution branches for $\mu = 0$ and plot them in figure 8. In figure 8, we have used $\kappa = 0$ as well (but see the discussion later, following equation (9.5)). All other parameters are the same as for figure 4.

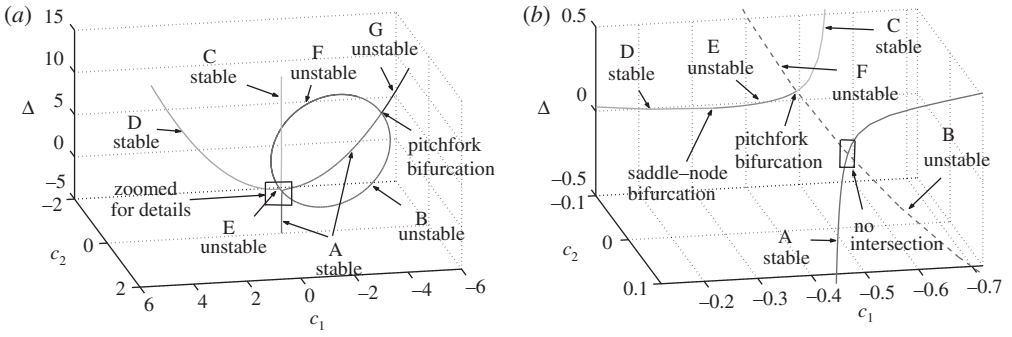

Figure 8. Bifurcation diagram for zero damping case. Parameters: $\kappa = 0$, $\mu = 0$ and $J = 0.6$. (*a*) Overall picture. (*b*) Zoomed portion of the overall picture showing bifurcation details.

In figure 8, the stable branch A remains intact for large negative Δ. However, branch A now loses stability via a subcritical pitchfork bifurcation[3] and continues as branch G. At the pitchfork point, two unstable branches, B and F, which now form a perfect ellipse (as will be demonstrated analytically later), meet branch A.

More interestingly, for large positive Δ, both branches C and D are stable. These branches meet, and also intersect the unstable branches B and F in what appears to be a pitchfork bifurcation. However, this suggests that either branch C or branch D must change stability prior to the pitchfork point, and this is indeed what happens. It is branch D which loses stability via yet another saddle–node bifurcation, changing to unstable branch E. Branch E, after a short distance, gains stability via a pitchfork bifurcation, meeting F and B. After the pitchfork point, stable branch C emerges. These issues are more clearly seen in the zoomed plot figure 8*b*. Representative plots of whirl orbits corresponding to these branches are provided in the electronic supplementary material.

Finally, note that the branch A is separated from the pitchfork point, and does *not* intersect the ellipse in that region. This gap exists owing to the non-zero *forcing* present in the system, and corresponds to the finite width near the base of a resonance peak for any oscillator forced near resonance; that width goes to zero as the damping goes to zero *and* the forcing amplitude goes to zero as well. So also, here, if we let damping *and* gravity go to zero, then the vertical part of A will merge with C (and both will shift sideways to merge with the Δ-axis, representing the trivial or zero solution). Simultaneously, the curved part of A, along with branches D, E and G, will make a perfect parabola (as we will demonstrate indirectly below) in the c_1–Δ plane, also passing through the origin. Finally, the ellipse will become indeterminate and turn into a paraboloid. In this sense, zero damping and small but non-zero gravity may be seen as leading to an imperfect version of three intersecting curves: a straight line, a parabola and an ellipse. Demonstration of the above features requires retaining a gravity forcing parameter F throughout the formulation, leading to longer expressions which we have avoided here (but verified separately). In this paper, we have taken gravity as given, and used $F = 1$ after scaling in terms of the small parameter ν.

[3]Note that, for $\mu = 0$, if (c_1, c_2) is a fixed point of equations (6.9) and (6.10), then so is $(c_1, -c_2)$. Non-zero damping breaks this symmetry, and breaks the pitchfork.

9. Analysis for zero damping

We now analytically consider the undamped case, using the first-order slow flow equations (6.9) and (6.10), whose fixed points were plotted for some choice of parameter values in figure 8. Our aim is to analytically establish the picture described above: that of an imperfect version of three mutually intersecting curves, namely a straight line, a parabola and an ellipse.

(*a*) *Straight line and parabola* ($c_2 = 0$)

We begin by setting $\mu = 0$ in the right-hand sides of equations (6.9) and (6.10) and then setting them to zero, obtaining

$$\frac{c_2}{2J-8}\Big(16+24c_2^2+24c_1+8\sqrt{4-2J}\Delta J-13J+24c_1^2-22Jc_2^2 - 22Jc_1^2-24Jc_1-16\sqrt{4-2J}\Delta\Big)=0 \tag{9.1}$$

and

$$\frac{1}{2J-8}\Big(-6-4\kappa+5J+12Jc_2^2-24c_2^2c_1+23Jc_1+36Jc_1^2+22Jc_2^2c_1 +8\sqrt{4-2J}\Delta-36c_1^2-12c_2^2-24c_1^3+22Jc_1^3-24c_1+2\kappa J + 16\sqrt{4-2J}\Delta c_1-4\sqrt{4-2J}\Delta J-8\sqrt{4-2J}\Delta Jc_1\Big)=0. \tag{9.2}$$

As equation (9.1) is identically satisfied for $c_2 = 0$, equation (9.2) with $c_2 = 0$ gives a relation between c_1 and Δ which describes the curves in the c_1–Δ plane

$$\Delta=\frac{-36{c_1}^2-6+22J{c_1}^3-24{c_1}^3+23Jc_1+36J{c_1}^2-4\kappa-24c_1+2\kappa J+5J}{4\sqrt{4-2J}(J-2)(2c_1+1)}. \tag{9.3}$$

Equation (9.3) describes the curves D, E, A, G and C of figure 8. In equation (9.3), at $c_1 = -1/2$ there is an asymptote parallel to the Δ-axis, giving the *straight line* portions of figure 8. Next, for large c_1, we replace $2c_1 + 1$ in the denominator with $2c_1$, and in the numerator retain only the terms cubic in c_1. This gives the *parabola*

$$\Delta=\frac{1}{8}\frac{(22J-24){c_1}^2}{\sqrt{4-2J}(-2+J)}. \tag{9.4}$$

As explained above, in the absence of gravity, we would have exactly a straight line and a parabola.

In equation (9.4), the coefficient of c_1^2 changes sign as J crosses $12/11$, which is within the parameter range of interest ($0 < J < 2$). In figures 6 and 8, we had used $J = 0.6 < 12/11$. For $J > 12/11$, the parabola bends in the opposite direction, as we will illustrate at the end of this section.

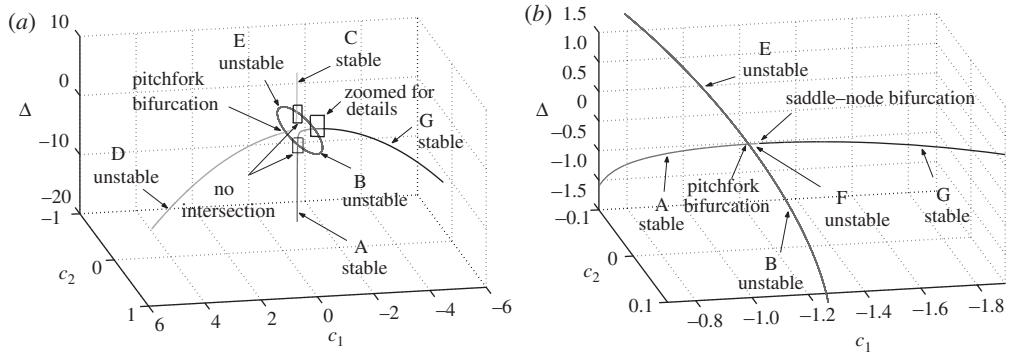

Figure 9. Bifurcation diagram for $J > 12/11$, with zero damping, showing the inversion of orientation of branches D, A and G. Parameters: $\kappa = 0$, $\mu = 0$ and $J = 1.25$. (*a*) Overall picture. (*b*) Zoomed portion of the left.

(*b*) *Ellipse* ($c_2 \neq 0$)

We now turn to the elliptical portion (branches B and F of figure 8). Here, $c_2 \neq 0$. Accordingly, we consider the expressions within parentheses in equations (9.1) and (9.2). Eliminating Δ, we find

$$4J^2c_1^2 + 4J^2c_2^2 + 8J(2-J)c_1 - 8\kappa J(2-J) + 8J - 6J^2 = 0. \tag{9.5}$$

The quadratic terms have identical positive coefficients, showing that it is in fact a circle (in the projection onto the $\Delta = 0$ plane). Note that κ here adjusts the size of the circle. With a little algebra, it can be shown that the radius of the circle remains positive for all $0 < J < 2$ and $\kappa \geq 0$ (as per our initial assumptions). Thus, the circle remains intact for all parameter values of interest. With some further algebra, c_2^2 can be eliminated between equations (9.1) and (9.2), giving a *linear* relationship between Δ and c_1, showing that non-zero-c_2 solutions lie on some plane. Finally, projecting the above circle, of equation (9.5), along the Δ direction onto that plane gives exactly an ellipse (no approximation).

(*c*) *Some results for* $J > 12/11$

We close this section with some final numerical results for $J > 12/11$, so that the change in the bending direction of the parabola described above may be seen. We take $J = 1.25 > 12/11$, in the zero damping limit. Results are plotted in figure 9. In addition to the change in the parabola's bending direction, there is also the movement of the saddle–node bifurcation point between branches D and E (see figure 8*b*). As J approaches 12/11 from below, this bifurcation point moves off to the far left side, taking large positive c_1 values; as J crosses 12/11, this bifurcation point reappears on the far right, i.e. at large negative c_1. Further increases in J bring the saddle–node bifurcation point once again to the vicinity of the pitchfork bifurcation. The stability of major portions of the parabolic branch, as depicted in the figures, reflects this movement of the saddle–node point.

10. Conclusions

We have presented a nonlinear study of an asymmetric, overhung rotor model due to Crandall & Brosens (1961), spinning near its gravity critical speed. The incorporation of nonlinearity, the treatment using the MMS and the subsequent detailed numerical and analytical investigation of the slow flow are all contributions of this paper.

The first-order slow flow verified the known unimportance of inertia asymmetry in gravity resonances; the second-order slow flow, however, demonstrated a weak but non-zero role of the same. The role of gyroscopic effects on maximum resonant amplitudes was examined and clarified. Weakly resonant effects were found even in the absence of asymmetry, something that linear analyses do not capture.

Future work in this direction may involve the next simplest nonlinear overhung rotor model, where the slender rotor portion is modelled as a beam. Such a model must include at least one more degree of freedom in each plane of bending, bringing in significant new complications.

References

Basu-Mandal, P., Chatterjee, A. & Papadopoulos, J. M. 2007 Hands-free circular motions of a benchmark bicycle. *Proc. R. Soc. A* **463**, 1983–2003. (doi:10.1098/rspa.2007.1849)

Bishop, R. E. D. & Mahalingam, S. 1965 Some experiments in the vibration of a rotating shaft. *Proc. R. Soc. Lond. A* **292**, 537–561. (doi:10.1098/rspa.1966.0152)

Bishop, R. E. D. & Parkinson, A. G. 1965 Second order vibration of flexible shafts. *Phil. Trans. R. Soc. Lond. A* **259**, 1–31. (doi:10.1098/rsta.1965.0052)

Brosens, P. J. & Crandall, S. H. 1961 Whirling of unsymmetrical rotors. *Trans. ASME, J. Appl. Mech.* **28**, 355–362.

Childs, D. 1993 *Turbomachinery rotordynamics: phenomena, modeling and analysis*. New York, NY: Wiley-Interscience.

Coleman, R. P. & Feingold, A. M. 1958 *Theory of self-excited mechanical oscillations of helicopter rotors with hinged blades*. NACA Report no. 1351, Langley Field, VA, ch. 2 and 3.

Crandall, S. H. & Brosens, P. J. 1961 On the stability of rotation of a rotor with rotationally unsymmetric inertia and stiffness properties. *Trans. ASME, J. Appl. Mech.* **28**, 567–570.

Den Hartog, J. P. 1956 *Mechanical vibrations*, 4th edn. New York, NY: McGraw-Hill.

Foote, W. R., Poritsky, H. & Slade Jr, J. J. 1943 Critical speeds of a rotor with unequal shaft flexibilities, mounted in bearings of unequal flexibility—I. *Trans ASME, J. Appl. Mech.* **10**, A77–A84.

Genta, G. 2005 *Dynamics of rotating systems*. New York, NY: Springer.

Hull, E. H. 1961 Shaft whirling as influenced by stiffness asymmetry. *Trans. ASME, J. Eng. Indust. B* **83**, 219–226.

Ishida, Y. 1994 Nonlinear vibrations and chaos in rotordynamics. *JSME Int. C Dyn. Control Robot. Design Manufact.* **37**, 237–245.

Ishida, Y., Liu, J., Inoue, T. & Suzuki, A. 2008 Vibrations of an asymmetrical shaft with gravity and nonlinear spring characteristics (isolated resonances and internal resonances). *ASME J. Vibrat. Acoust.* **130**, 041004-1–041004-8.

Kane, T. R., Ryan, R. R. & Banerjee, A. K. 1987 Dynamics of a cantilever beam attached to a moving base. *J. Guid. Control Dyn.* **10**, 139–151. (doi:10.2514/3.20195)

Kondo, Y. & Kimura, H. 1991 Study on the vibration of an asymmetrically elastic rotating shaft—some considerations on the phase response and whirling. *Mem. Shonan Inst. Technol.* **25**, 29–39.

Mahadevan, P., Jog, C. S. & Chatterjee, A. 2008 Modal projections for synchronous rotor whirl. *Proc. R. Soc. A* **464**, 1739–1760. (doi:10.1098/rspa.2007.0139)

Nagasaka, I., Ishida, Y. & Liu, J. 2008 Forced oscillations of a continuous asymmetrical rotor with geometrical nonlinearity (major critical speed and secondary critical speed). *ASME J. Vibrat. Acoust.* **130**, 031012-1–031012-7.

Nandakumar, K. & Chatterjee, A. 2005 Resonance, parameter estimation, and modal interactions in a strongly nonlinear benchtop oscillator. *Nonlinear Dyn.* **40**, 149–167. (doi:10.1007/s11071-005-4228-3)

Nayfeh, A. H. & Mook, D. T. 1979 *Nonlinear oscillations*. New York, NY: John Wiley & Sons.

Rajalingham, C., Bhat, R. B. & Xistris, G. D. 1993 Influence of external damping on the stability and response of a horizontal rotor with anisotropic bending stiffness. *Tribol. Trans.* **36**, 393–398. (doi:10.1080/10402009308983175)

Rao, J. S. 1983 *Rotor dynamics*. New Delhi, India: New Age International Publishers.

Rao, J. S. & Sreenivas, R. 2003 Dynamics of asymmetric rotors using solid models. In *Proc. International Gas Turbine Congress 2003, Tokyo, Japan, 2–7 November 2003*.

Sakata, M., Endo, M. & Kishimoto, K. 1983 Secondary critical speed of flexible rotors with inertia slots. *J. Sound Vibrat.* **87**, 61–70. (doi:10.1016/0022-460X(83)90439-X)

Smith, D. M. 1933 The motion of a rotor carried by a flexible shaft in flexible bearings. *Proc. R. Soc. Lond. A* **142**, 92–118. (doi:10.1098/rspa.1933.0158)

Taylor, H. D. 1940 Critical-speed behavior of unsymmetrical shafts. *Trans. ASME, J. Appl. Mech.* **7**, A71–A79.

Thomsen, J. J. 1995 Chaotic dynamics of the partially follower-loaded elastic double pendulum. *J. Sound Vibrat.* **188**, 385–405. (doi:10.1006/jsvi.1995.0600)

Yamamoto, T. & Ōta, H. 1963 On the vibrations of the shaft carrying an asymmetrical rotating body. *Bull. Jpn. Soc. Mech. Eng.* **6**, 29–36.

Yamamoto, T., Ishida, Y., Ikeda, T. & Yamamoto, M. 1982 Nonlinear forced oscillations of a rotating shaft carrying an unsymmetrical rotor at the major critical speed. *Bull. Jpn. Soc. Mech. Eng.* **25**, 1969–1976.